Case Studies in Thermal Engineering 28 (2021) 101583

Contents lists available at ScienceDirect

Case Studies in Thermal Engineering

journal homepage: www.elsevier.com/locate/csite

A holistic approach to thermal-hydraulic design of 3D manifold microchannel heat sinks for energy-efficient cooling

Daeyoung Kong [a,1], Yunseo Kim [a,1], Minsoo Kang [a], Erdong Song [b], Yongtaek Hong [c], Han Sang Kim [c], Kyupaeck Jeff Rah [c], Hyoung Gil Choi [c], Damena Agonafer [b], Hyoungsoon Lee [a,d,*]

[a] *Department of Intelligent Energy and Industry, Chung-Ang University, Seoul, 06974, South Korea*
[b] *Department of Mechanical Engineering & Materials Science, Washington University in Saint Louis, Saint Louis, MO, 63130-4899, USA*
[c] *Global Technology Center, Samsung Electronics Co., Ltd., Suwon, 16677, South Korea*
[d] *School of Mechanical Engineering, Chung-Ang University, Seoul, 06974, South Korea*

A R T I C L E I N F O

Keywords:
Thermal management
Manifold microchannel
Thermal performance index
Electronics cooling

A B S T R A C T

Manifold microchannel heat sinks (MMCHSs) have attracted attention for the thermal management of high-performance electronics owing to their high heat dissipation rate and low pressure drop compared to conventional microchannels. This study used a full 3D conjugated simulation to analyze the effects of changes in the geometry and operating environment on the thermal and hydraulic performance of MMCHS. The findings provide a holistic view of MMCHS design for performance improvement. Twelve manifold geometries were designed by changing the direction and width of the manifold outlet in each case. Using water as the working fluid, we evaluated each manifold's thermal and hydraulic performance in the flow rate range of 100–500 g/min, and compared their thermal resistances per unit pumping power to determine the most efficient manifold structure for each operating environment. Compared to a conventional microchannel, the MMCHS reduced the thermal resistance by up to 47% and the pressure dropped by up to 90%, depending on the geometry. The thermal performance index (TPI), which relates thermal performance to pressure drop, was improved by 139% in the current MMCHS design over the TPI of a conventional microchannel. This sizeable improvement resulted from the excellent temperature uniformity and shortened the fluid flow path in the microchannel.

1. Introduction

The dramatic advances in microfabrication and packaging technologies have aided in the miniaturization of high-performance electronic devices. As the devices become smaller, the need to dissipate the heat generated becomes drastically greater to avoid premature failure and improve the reliability of the devices [1]. Various types of high-heat-flux cooling schemes have been proposed, such as mini/microchannel [2–5], jet impingement [6–8], spray cooling [9–11], microchannel with secondary flow [12,13], evaporative cooling [14], micro-pin fin [15–17], electrospray [18,19], liquid metal [20], and nanofluids [21]. The microchannel heat sink design [22] has been widely used in high-heat flux electronic applications because it provides superior heat transfer performance and is

* Corresponding author. Department of Intelligent Energy and Industry, Chung-Ang University, Seoul, 06974, South Korea.
E-mail address: leeh@cau.ac.kr (H. Lee).
[1] Contributed equally to this work.

https://doi.org/10.1016/j.csite.2021.101583
Received 21 July 2021; Received in revised form 29 September 2021; Accepted 23 October 2021
Available online 24 October 2021

Nomenclature

A	area
C_p	specific heat
COP	coefficient of performance
D_h	hydraulic diameter
g	acceleration due to gravity
H	height
k	thermal conductivity
L	total chip length
$\dot{m}$	mass flow rate
P_{pump}	pumping power
ΔP	pressure drop
q	heat dissipation rate
q''	heat flux
R	thermal resistance
T	temperature
$\bar{T}_f$	mean fluid temperature
$\bar{T}_h$	mean heater temperature
t	thickness
u	fluid velocity
W	width

Greek symbols

Γ	effective diffusivity
θ	tilt angle of manifold
μ	dynamic viscosity
ρ	density
ω	specific dissipation rate

Subscripts

b	base
ch	channel
in	inlet
k	turbulence kinetic energy
m	manifold
max	maximum
out	outlet
p	pump
tot	total
w	wall

easily fabricated owing to its structural simplicity. However, its energy efficiency is low because a small hydraulic diameter necessitates a high pumping power, increasing the frictional pressure drop. Additionally, non-uniform temperature along the flow direction leads to serious reliability concerns, which is a major disadvantage in electronic systems.

The manifold microchannel heat sink (MMCHS) was first proposed by Harpole et al. [23]. It provides effective heat transfer and a low pressure drop by placing additional channels above the MCHS and orthogonal to its length. Half of the manifold channels are inlets, and the other half are outlets alternating along the length of the microchannel. The inlet channels distribute cold working fluid over the entire heated area, and the outlet channels remove the fluid after it has absorbed heat. Fig. 1 shows a conceptual schematic of the simplest geometric configuration of an MMCHS. The working fluid is first introduced to the inlet channels on one side of the manifold, and portions of it flow down into each microchannel as it moves long the channel. Then, it flows beneath the channel wall and upwards into the adjacent outlet channels. Thermal engineers have fabricated the complex morphology of MMCHS through machining [24–26], microfabrication [27–31], and additive manufacturing technology [32–34]. Because the manifold has a relatively large cross-sectional area, and the design shortens the effective flow path through the microchannel, less pumping power is needed than for a conventional microchannel heat sink. Moreover, because the working fluid is forced down and collides with the bottom, the thin thermal boundary layer created by jet impingement improves heat transfer. As a result, the MMCHS has aroused great interest in fields using high heat fluxes, such as defense electronics, laser weapons, data centers, and power electronics. However, predicting its thermal and hydraulic performance is difficult owing to the many design parameters inherent in its structural complexity. In this study, using full 3D conjugate simulation and statistical parametric analysis, we elucidated the effects of geometrical and operational parameters on the thermal and hydraulic performance of the design from a holistic viewpoint. We assessed 12 geometries with varying

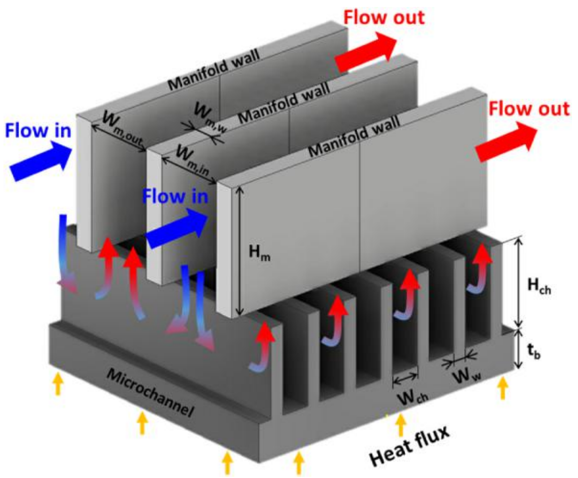

Fig. 1. Conceptual schematic of manifold microchannel heat sink (MMCHS).

flow rates and investigated the corresponding pressure drops and thermal resistances.

2. Methods

2.1. Design and operational variables of manifold microchannel heat sink

Fig. 2 shows the four manifold geometrical configurations of MMCHS, which are divided into two classes, depending on whether the in-and-out-flows are parallel or perpendicular to each other. Fig. 2(a) shows a configuration in which the inlet and outlet of the manifold flows move horizontally [24–27], whereas Fig. 2(b) shows the fluid entering via two opposing horizontal inlets and flowing out vertically [28–30]. The horizontal flow configuration in Fig. 2(a) was subdivided into Cases A and B. The basic conventional manifold, Case A, has a constant cross-sectional manifold area, but the fluid velocity decreases gradually with the flow direction within the manifold [24–26]. Alternatively, Case B has manifold walls that taper according to the flow direction to compensate for the

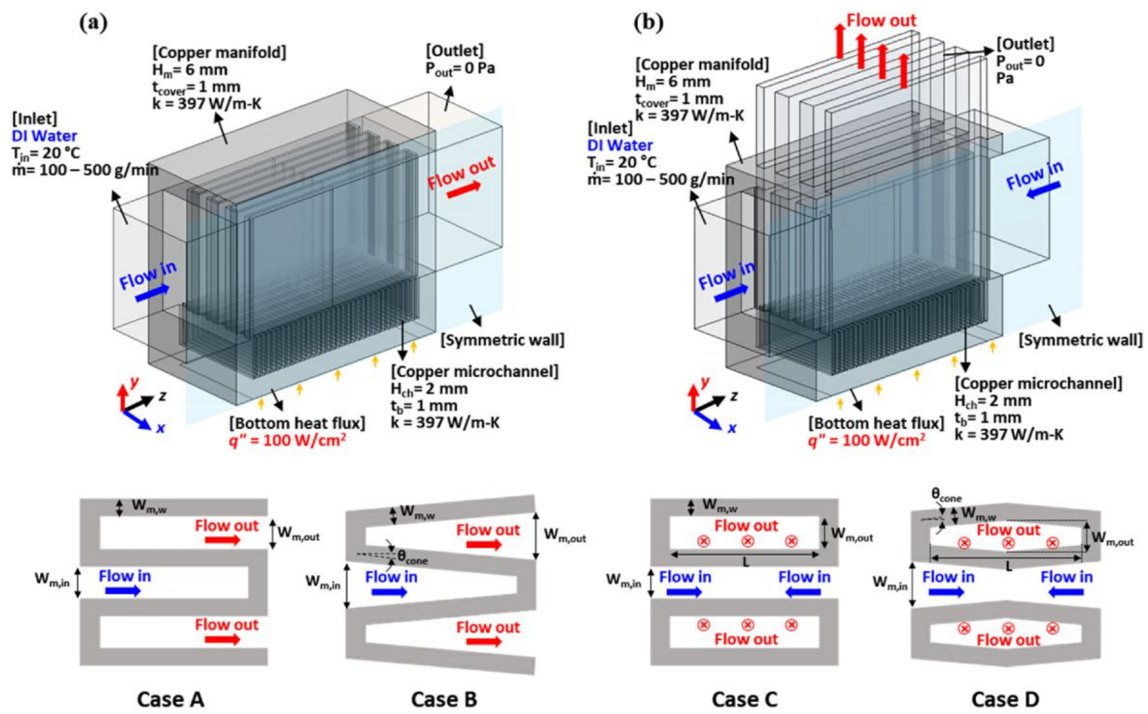

Fig. 2. Computational domains and boundary conditions of four manifold configurations.

reduction in fluid velocity [27,31,35]. For the vertical flow configurations in Fig. 2(b), the Case C manifold is composed of parallel manifold walls that form a rectangular outlet to reduce the flow path while the fluid is exiting [28–30]. The Case D manifold is newly devised: we used a closed and tapered manifold wall to create a uniform flow velocity distribution entering the microchannel, for the same reason as in Case B. In this study, to focus on the effects of changes in the configuration of the manifold, we used a fixed microchannel design with dimensions of $W_{ch} = 200$ μm, $H_{ch} = 2000$ μm, and $W_w = 100$ μm. Table 1 lists the shape information of the manifolds and microchannels used in this study. The commercial CFD software ANSYS Fluent 19.2 was used to perform the conjugated simulation, and the analysis assumed a steady-state fluid with no radiation effect. The range of the Reynolds number inside the channel at the maximum flow rate is $Re_{ch} = 68$–125 (Re_{ch} is defined as $Re_{ch} = \rho u_{ch} D_{h,ch}/\mu$), which is a laminar flow; however, a shear stress transport (SST) k–ω turbulence model was applied to account for turbulence as the fluid moved in and out of the manifold and microchannel boundary [36]. The detailed constitutive continuity, momentum, energy, k, and ω equations are provided in the supplementary material (Appendix A).

2.2. Conjugate numerical model

To minimize computational effort, half-symmetric computational domains were used because the full-scale geometry was symmetric with respect to the inflow direction of the manifold. The manifold and microchannel were composed of a solid domain connected to a body, and a fluid domain was formed by filling the space inside the MMCHS. To avoid end effects, the inlet and outlet were extended by 4 mm. Copper was chosen as the material for the solid domain, including the manifold and microchannel, and water was used as the working fluid. The thermophysical property values for the water and copper used in the simulations are summarized in Table 2. Third-order and fourth-order polynomial functions in the fluid properties were adopted to improve the simulation accuracy.

Five mass flow rates, from 100 to 500 g/min, were set as inlet mass flow conditions, and the inlet fluid temperature was set to an ambient temperature of $T_{in} = 20\ ^{\circ}$C. A gauge pressure of 0 Pa was used for the outlet conditions. A constant heat flux boundary condition of $q'' = 100$ W/cm^2 was used for the 10×5 mm^2 heated surface. For the solid–liquid interface, a non-slip and coupled wall boundary condition was used. The remaining boundaries were subjected to a single-phase simulation under adiabatic conditions. The detailed computational methods and controls are shown in Table 3.

Hexahedral elements generated by ANSYS meshing were used to obtain high accuracy and reduce the calculation time. Thin layers of the element were created in the solid–fluid interfaces between the microchannel and manifold to improve the accuracy of calculations in capturing rapid velocity changes at the interface. The mesh independence was evaluated for several elements ranging from a minimum of 1 million to a maximum of 10 million cells, and the results are summarized in Table 4. Based on the grid independence test, all simulation domains were introduced and calculated using more than 10 million elements.

3. Results and discussion

3.1. Flow uniformity in microchannels

The thermal resistance of a single-phase forced convective flow depends highly on its velocity field. Hence, the velocity distribution influenced the temperature distributions. Fig. 3 shows the distributions of the average velocity in each microchannel for the four manifold configurations. Case A has a relatively even flow distribution at flow rates from 100 to 300 g/min, which is relatively low. However, as the total flow rate increased, the channels near the rear (farthest from the inlet) started to experience a higher velocity than the channels near the front. This difference stems from the increased flow inertia, which creates a high pressure near the rear by flow stagnation, thus forcing fluid into the adjacent channels. The effect of the outlet width on the flow distribution is shown in Cases A1, A2, and A3. As the outlet width increases, flow maldistribution becomes more apparent because of the correspondingly increased inlet velocity, a consequence of the fact that the total number of inlet manifolds within the fixed total width decreases. In Case B, the channels in the front tend to have higher velocities than the channels in

Table 1
Dimensions of 3D manifold-microchannel geometries.

Case		Manifold					Microchannel (MC)		
		H_m [μm]	$W_{m,w}$ [μm]	$W_{m,in}$ [μm]	θ_{cone} [degree]	$W_{m,out}$ [μm]	H_{ch} [μm]	W_{ch} [μm]	W_w [μm]
Case A	A1	6000	150	450	0°	505	2000	200	100
	A2					905			
	A3					1405			
Case B	B1				1°	854			
	B2					1254			
	B3					1754			
Case C	C1				0°	10,000 × 505			
	C2					10,000 × 905			
	C3					10,000 × 1405			
Case D	D1				1°	10,000 × 680			
	D2					10,000 × 1080			
	D3					10,000 × 1580			

Table 2
Thermophysical properties of water and copper.

	Fluid	Solid
	Water	Copper
μ [N·s/m^2]	$-1.421 \times 10^{-11}T^4 - 2.021 \times 10^{-8}T^3 + 1.082 \times 10^{-5}T^2 - 2.590 \times 10^{-3}T + 0.234$	–
k [W/(m·K)]	$2.287 \times 10^{-8}T^3 – 3.120 \times 10^{-5}T^2 + 1.413 \times 10^{-2}T - 1.44$	388
ρ [kg/m^3]	$1.054 \times 10^{-5}T^3 – 1.359 \times 10^{-2}T^2 – 5.034T + 425.3$	8978
C_p [J/(kg·K)]	$-3.230 \times 10^{-5}T^3 + 4.150 \times 10^{-2}T^2 – 16.45T + 6254$	381

Table 3
Computational methods and controls.

Discretization Method	
Pressure–Velocity Coupling	Semi-Implicit Method for Pressure Linked Equation (SIMPLE)
Gradient	Least-Squares Cell-Based
Pressure	Second-Order
Momentum	Second-Order Upwind
Turbulent Kinetic Energy	First-Order Upwind
Specific Dissipation Rate	First-Order Upwind
Energy	Second-Order Upwind

Table 4
Results of the grid independence test.

Index	Number of elements	Pressure drop [Pa]	Average heater temperature [°C]	$\left(\frac{\Delta P_n - \Delta P_{n-1}}{\Delta P_n}\right) \times 100[\%]$	$\left(\frac{T_{h,n} - T_{h,n-1}}{T_{h,n}}\right) \times 100[\%]$
1	1,285,462	39.87	50.65	null	null
2	3,261,238	40.92	50.42	2.57	0.46
3	6,743,247	41.86	50.34	2.25	0.16
4	10,221,981	42.27	50.31	0.97	0.06

the rear. The tapered manifold structure provides a larger flow inlet area at the channels near the front, resulting in a lower flow resistance. This effect appears to be dominant at low flow rates. However, as the total flow rate and outlet width increased, so did the effect of inertia, which drives more flow to the channels near the rear and is also suspected to be dominant. Consequently, the channels near the inlet and outlet of the manifold exhibited higher velocities. Fig. 3(c) and (d) show the relatively even flow distributions of Cases C and D, which have different configurations. In these cases, the fluids are introduced via inlets on both sides of the manifold and collide at the center of the manifold, where flow stagnation creates high pressure. As a result, the channels near the center show higher velocity, and this inequality becomes more severe as the inertia increases at higher flow rates and larger outlet widths.

Case D had a symmetrically reduced inlet manifold structure. This design provides a lower flow resistance at the sides of the manifold and mitigates the inequality caused by flow inertia. This effect prevails over the effect of inertia at low flow rates. However, in contrast to Case B, the tapered structure decreases the overall cross-sectional area of the manifold. Thus, the severe effect of inertia, which is suspected to dominate in creating flow maldistribution at high flow rates.

3.2. *Temperature distribution of heated surface*

Fig. 4 represents the cross-sectional temperature contours of the inlet manifold for different manifold cases at a mass flow rate of 100 g/min. The temperature is non-uniform because sensible heat is conducted from the outlet plenum. In cases A and B, because the outlet plenum is located on the right side of the manifold, the temperature is higher at the rear part of the module. To the contrary, cases C and D show symmetric temperature profiles because their outlet plenums are on the top center of the module. It is also clear that the fluid temperature in the stagnation zone rises significantly due to low heat transfer coefficient. Fig. 5 shows surface temperature contours of different cases of manifold at different flow rates, and Fig. 6 shows the distribution of temperature at the centerline and the differences between the maximum and minimum temperature. For a given geometry, it is evident that better temperature uniformity is attained by increasing both the total flow rate and the outlet width. This tendency reflects the enhanced convective heat transfer with increased velocity. As illustrated in Figs. 5(a) and 6(a), in Case A, the hot spot tends to be located behind the centerline at low flow rates. Flow maldistribution mitigates this tendency by supplying more fluids to the channels at the rear side, resulting in a higher heat transfer coefficient despite the higher fluid temperature. The flow maldistribution becomes severe as both the flow rate and outlet width are increased, thus the local hotspot moves toward the inlet of the manifold. In contrast, in Case B, which tends to supply more fluid to the front owing to the tapered manifold walls, the hot spot occurs further downstream of the flow direction because the convective heat transfer is deteriorated by the lower flow rate introduced into the channel downstream (Figs. 5(b) and 6(b)). As a result, Case B exhibits relatively higher temperature differences than those of other cases, except for case 1 cases where

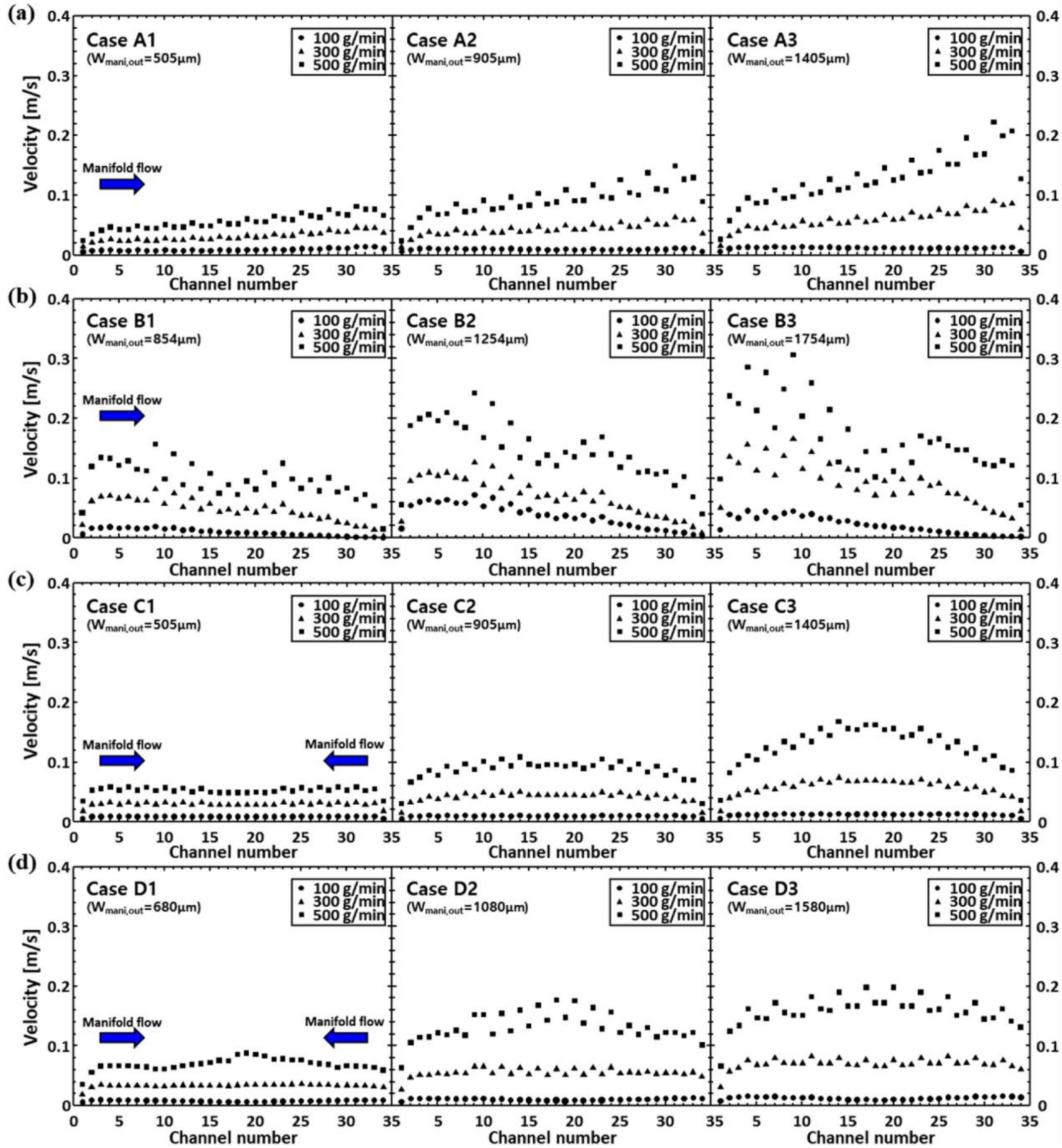

Fig. 3. Average velocity distributions from each microchannel for four manifold configurations.

the flow inequality of case A is not severe.

Cases C and D exhibit relatively even temperature distributions compared with the other cases. In these configurations, the effect of conduction through the manifold is insignificant owing to the configuration of the outlet plenum, and the flow distribution is more uniform because they have inlets at both ends of the manifold. The hot spots are at the center of the heated surfaces because the hot fluids mostly flow to the channels near the center, slightly elevating the temperature of the heated surface at the centerline. At low flow rates, there is little difference between Cases C and D. However, at high flow rates, Case D shows a slightly lower temperature difference because the channels in the centers start to experience higher velocities owing to the small cross-section at the center.

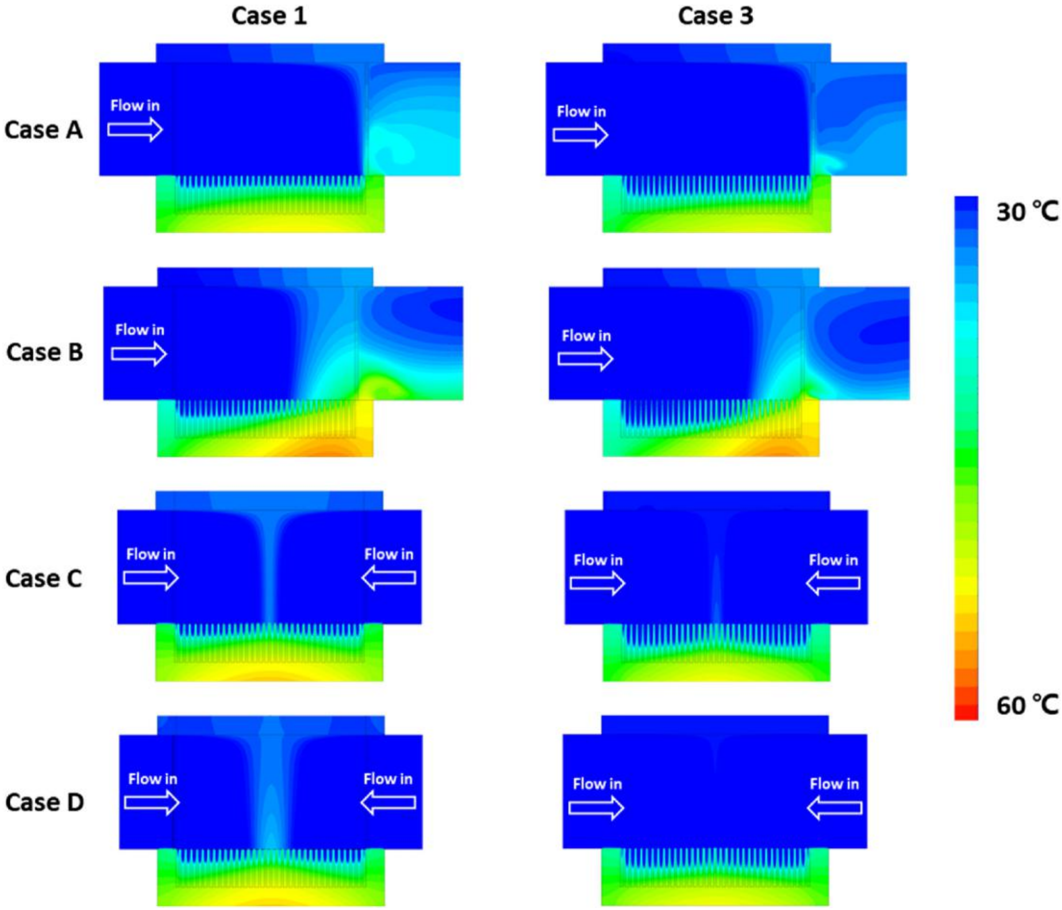

Fig. 4. Cross-sectional temperature contours of 3D manifold inlets for different manifold cases at a mass flow rate of 100 g/min.

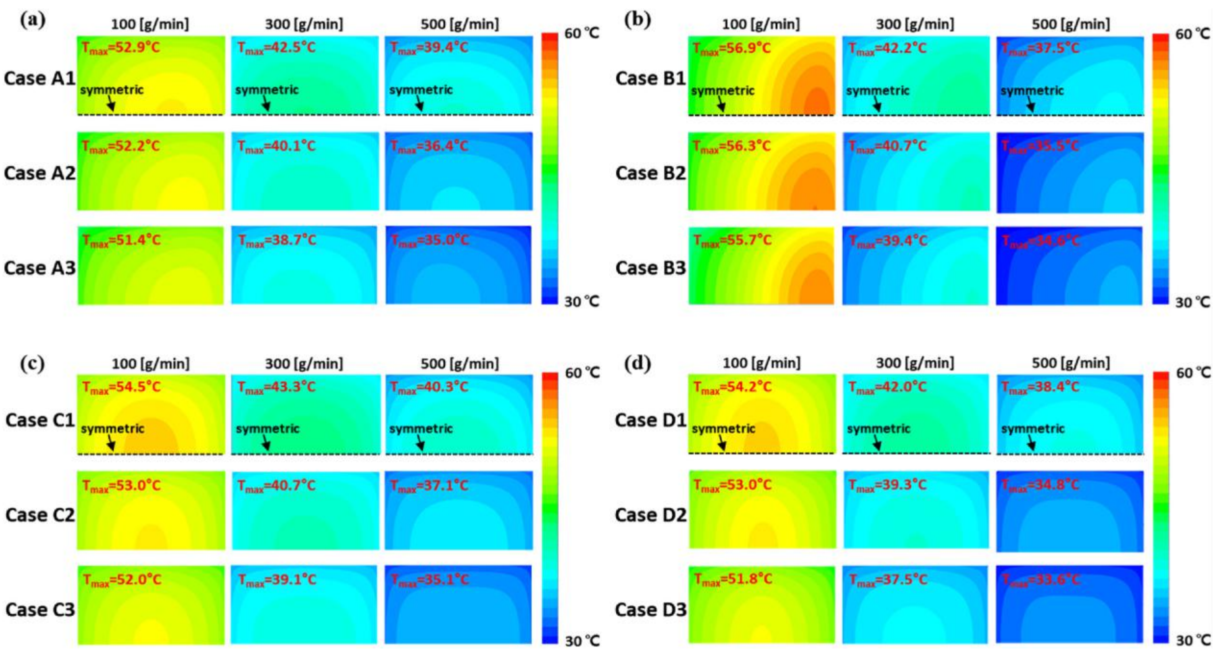

Fig. 5. ((a)–(d)) Contours of the surface temperature of different manifold geometries for three mass flow rates.

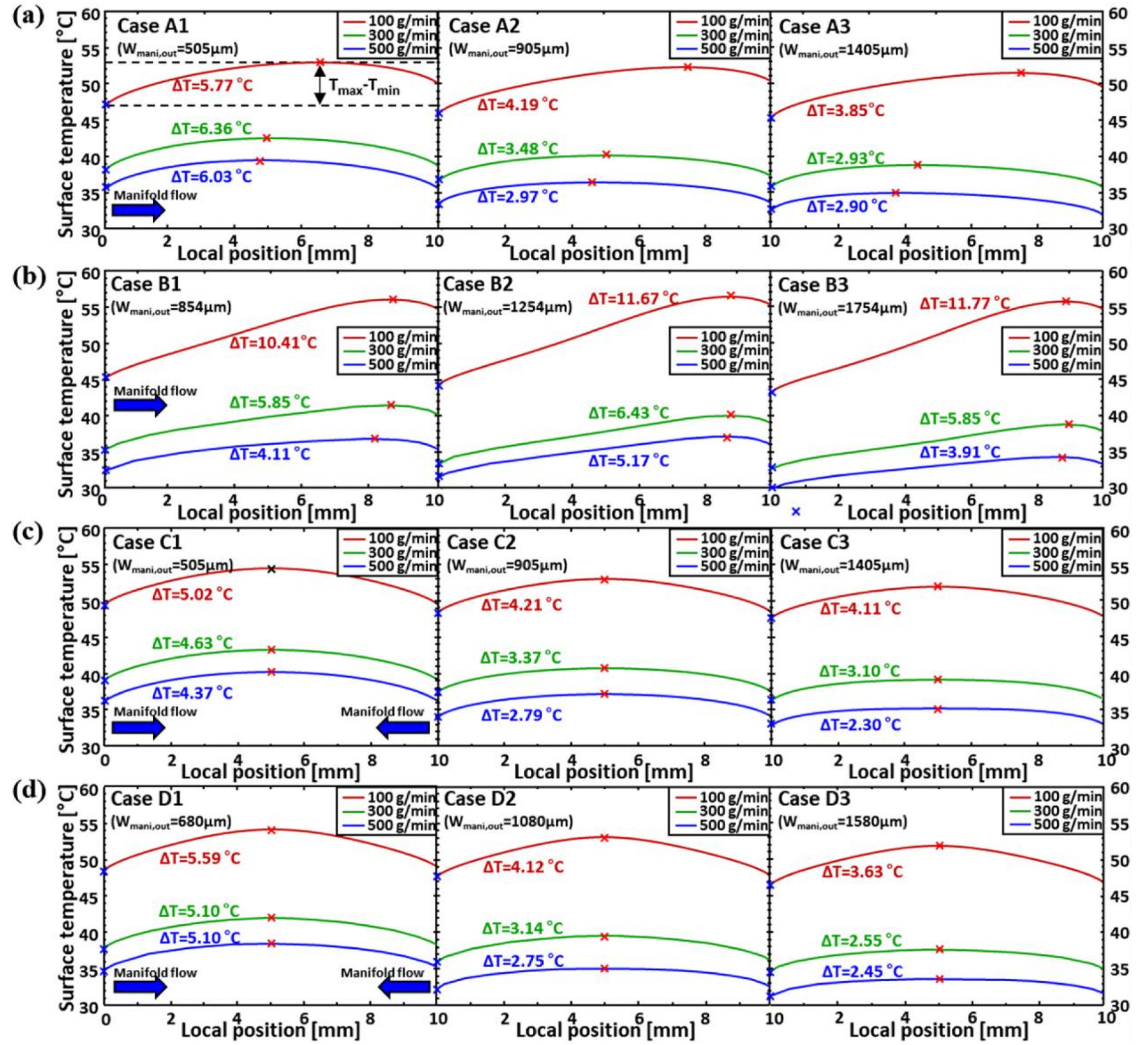

Fig. 6. Surface temperature profiles for different manifold outlet widths.

3.3. Total thermal resistance and pressure drop

To holistically investigate the thermal and hydraulic performance changes that widen the outlet of each manifold configuration, we plotted the thermal resistance and pressure drop for each flow rate considered above, with the results shown in Fig. 7. Here, the

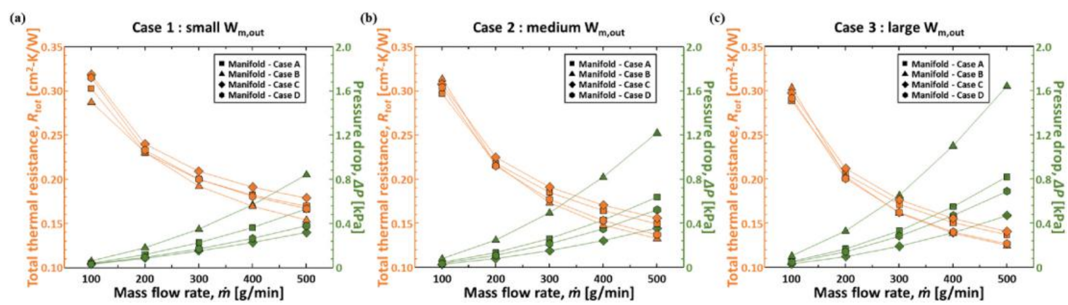

Fig. 7. Total thermal resistance and pressure drop vs. mass flow rate for three widths of manifold outlets and four manifold configurations.

thermal resistance is defined based on the average temperature of the heated surface.

$$R_{tot} = \frac{\overline{T}_{bot} - T_{in}}{q''}, \tag{4}$$

where the inlet temperature and heat flux were fixed at $T_{in} = 20\ ^{\circ}C$ and $q'' = 100\ W/cm^2$, respectively. As the flow rate increased, tradeoffs in the trends of thermal resistance and pressure drop were observed for each manifold configuration. The thermal resistance is generally highest in Case C, followed by Cases A and D, and is the lowest in Case B, which shows excellent heat transfer performance owing to the high flow velocity and high flow uniformity in each microchannel. However, the pressure drop is highest in Case B, lower in Cases A and D, and lowest in Case C. The larger pressure drops in Cases A and B arise from their higher inlet velocities than those of Cases C and D, which are affected by a sudden contraction between the inlet plenum and manifold. Additionally, the tapered MMCHSs, such as Cases B and D, showed better thermal resistance than the other two MMCHSs, but the pressure drop was relatively large because the tapered manifold walls reduced the cross-sectional area of the manifold inlet. This pressure drop could be a concern because it may increase the pumping power required to cool the heat source. Moreover, as the width of the manifold outlet expands, the number of manifold inlets and outlets decreases, resulting in increased fluid velocity at each manifold and an increased heat transfer rate and pressure drop. It was confirmed that as the manifold outlet widened, the thermal resistance was decreased by up to 17.7%–24.0% for each configuration, while the pressure drop increased by up to 46.5%–94.9%, as shown in Fig. 7. Additionally, the changes in the thermal and hydraulic performance of the MMCHS with different heat fluxes are provided in the supplementary material (Appendix B).

Fig. 8(a) shows the simulation results for the total thermal resistance and pressure drop for the four manifold configurations, and the comparable results for the thermal performance and pressure drop in the case of microchannels only. Compared to a microchannel heat sink of the same material, copper, the hot spot temperature of all MMCHSs decreased because of the jet impingement effect from the manifold, resulting in low thermal resistance, as shown in Fig. 8(a). Additionally, the low thermal resistance led to a significantly improved the pressure drop because of the shortened flow path of the fluid inside the microchannel. In terms of the shape of the manifold, the tapered manifolds, such as Cases B and D, show relatively lower thermal resistance than the parallel manifold Cases A and C. The angled manifold wall led to a uniform fluid flow distribution in the microchannel, which lowered the overall surface temperature, as shown in Fig. 6. However, compared to the parallel manifold, the pressure drop increased as the flow path in the tapered manifold itself narrowed. Meanwhile, Cases C and D with two manifold inlets have the advantage of a large manifold outlet compared to Cases A and B, so the pressure drop is greatly reduced.

Because of the inverse relationship between pressure drop and thermal resistance, a thermal performance index (TPI) was adopted to quantitatively express the relationship between the thermal performance and the pumping power required by the MMCHS. Here, TPI can be defined as the ratio of the pressure drop and heat transfer performance of the four cases of MMCHSs compared to the microchannel heat sink alone, which is a reference heat spreader [37] expressed as follows:

$$TPI = \frac{R_{tot,\mu-ch}/R_{tot}}{\left(\Delta P/\Delta P_{\mu-ch}\right)^{1/3}}. \tag{14}$$

where $R_{tot,\mu\text{-}ch}$ and $\Delta P_{tot,\mu\text{-}ch}$ are the thermal resistance and pressure drop, respectively, when only the microchannel heat sink is used. Based on TPI of one for the microchannel, the overall TPI of the MMCHS was 115% on average, as shown in Fig. 8(b). This result confirms the basic premise that it is possible to design an MMCHS with improved thermal characteristics by adding an extra manifold structure above the existing microchannel. TPI for each manifold case was calculated over the total flow rate, and the TPI of Case C had the highest values, identifying it as the most efficient MMCHS. Although the Case B manifold had superior heat transfer performance, it showed the lowest TPI owing to the rapidly elevated pressure drop, as shown in Fig. 7. Additionally, the manifolds with double-side inlets, Cases C and D, showed relatively low pressure drops and thermal resistances owing to the geometric advantage of having a wide vertical manifold outlet and uniform flow distribution inside the microchannel. For Cases C and D, the average TPI was 13% and 26% higher than that of Cases A and B, respectively.

Additionally, the coefficient of performance (COP), defined as the ratio of the heat dissipation rate to the pumping power ($COP = q/P_{pump}$), was compared for all four manifold configurations, including results from several experimental studies in the literature. In this study, the heat dissipation rate was fixed at 100 W. Fig. 9 shows the relationship between the COP and the pumping power of the four manifold configurations. For the same COP, the pumping power was lower in all MMCHSs than in the microchannel heat sink. The manifold of Case B, which demonstrates the lowest thermal resistance, requires increased pumping power because of the rapidly increasing pressure drop, and consequently, it has a low COP. Alternatively, Cases C and D MMCHSs, with two manifold inlets, require lower pumping power and have a higher COP than MMCHSs with single manifold inlets, owing to their excellent pressure drops.

4. Conclusions

We conducted numerical simulations of single-phase flow to compare the thermal and hydraulic performance of 12 manifold configurations in manifold microchannel heat sinks. MMCHSs made of copper, with water as the working fluid, were used in this study. The thermal and hydraulic performance of each MMCHS was also evaluated and compared by varying the width of each manifold outlet for mass flow rates ranging from 100 to 500 g/min at a fixed heat flux of 100 W/cm^2. The key findings of this study are as follows:

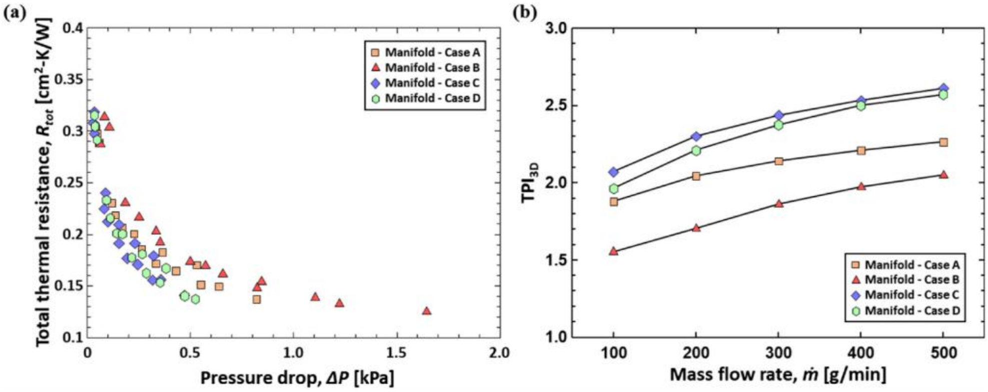

Fig. 8. (a) Total thermal resistance versus pressure drop and (b) thermal performance index (TPI) for the four manifold configurations, with the microchannel values as a reference.

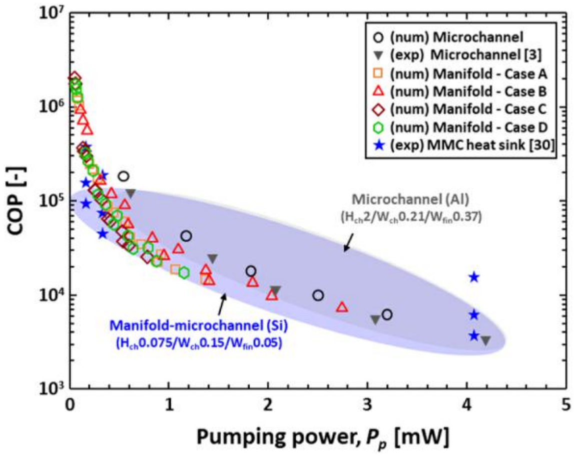

Fig. 9. Coefficient of performance and pumping power for four manifold designs. The open symbols are the numerical results for each manifold case, and solid symbols are thermal experimental data from Refs. [3,30].

(1) In configurations A and B, which have parallel manifold flows, the flow in each microchannel was maldistributed because the pressure was unevenly applied to the inside of the microchannel owing to the flow inertia of the fluid along with the manifold. Therefore, the local temperature of the heated surface of Cases A and B increased gradually, resulting in a relatively large increase in the hot-spot temperature.
(2) For Cases C and D, which have manifold inlets at opposing ends and outlets in the vertical direction, the flow path inside the manifold is reduced by half, and the pressure drops are decreased over those in Cases A and B, and the fluid flow inside the microchannel is evenly distributed. These configurations exhibit uniform microchannel flows and equally distributed surface temperatures. Furthermore, the flow rate was concentrated in the center of the MMCHS as the mass flow rate increased, reducing the hot-spot temperature.
(3) By using tapered manifold walls, as in Cases B and D, the flow path into the manifold was narrowed to equalize the pressure applied to the microchannel, and the flow was distributed equally. These cases can maintain a lower hot-spot temperature than Cases A and C when the mass flow rate increases.
(4) To reduce the thermal resistance to the heat flux generated by the heat source, Case B is preferable because it can achieve a high heat transfer rate instead of a relatively high pressure drop at a low flow rate ($\dot{m} < 300$ g/min). For a high flow rate ($\dot{m} \geq 300$ g/min), Case C, with a low pressure drop and uniform temperature distribution, is the most appropriate manifold configuration.

CRediT authorship contribution statement

Daeyoung Kong: Conceptualization, Methodology, Investigation, Data curation, Writing – original draft. **Yunseo Kim:** Investigation, Data curation, Writing – original draft. **Minsoo Kang:** Investigation, Data curation. **Erdong Song:** Formal analysis, Writing – review & editing. **Yongtaek Hong:** Supervision. **Han Sang Kim:** Supervision. **Kyupaeck Jeff Rah:** Supervision. **Hyoung Gil Choi:** Supervision. **Damena Agonafer:** Supervision, Writing – review & editing. **Hyoungsoon Lee:** Project administration, Supervision, Writing – review & editing.

Declaration of competing interest

The authors declare that they have no known competing financial interests or personal relationships that could have appeared to influence the work reported in this paper.

Acknowledgments

This work was supported by the Global Technology Center, Samsung Electronics Co., Ltd., and the Chung-Ang University Research Scholarship Grants in 2019.

Appendix C. Supplementary data

Supplementary data to this article can be found online at https://doi.org/10.1016/j.csite.2021.101583.

Appendix A. Conservation equations of CFD simulations

The constitutive continuity, momentum, energy, k, and ω equations are as follows:
Continuity equation:

$$\frac{\partial}{\partial x_i}(\rho u_i) = 0, \tag{1}$$

Momentum equation:

$$\frac{\partial}{\partial x_j}(\rho u_i u_j) = \frac{\partial p}{\partial x_i} + \frac{\partial}{\partial x_j}\left(\mu \frac{\partial u_i}{\partial x_j} - \rho \overline{u_i' u_j'}\right), \tag{2}$$

Energy equation:

$$\frac{\partial}{\partial x_i}(\rho u_i T) = \frac{\partial}{\partial x_i}\left(\frac{\mu}{\Pr}\frac{\partial T}{\partial x_i}\right), \tag{3}$$

k equation:

$$\frac{\partial}{\partial x_i}(\rho k u_i) = \frac{\partial}{\partial x_j}\left(\Gamma_k \frac{\partial k}{\partial x_j}\right) + G_k - Y_k, \tag{4}$$

ω equation:

$$\frac{\partial}{\partial x_i}(\rho \omega u_i) = \frac{\partial}{\partial x_j}\left(\Gamma_\omega \frac{\partial \omega}{\partial x_j}\right) + G_\omega - Y_\omega, \tag{5}$$

where Γ_k and Γ_ω are the effective diffusion terms of k and ω, respectively, and G and Y are the generation and dissipation terms, respectively.

Appendix B. Performance difference with respect to the increase in heat flux

The results of the thermal resistance and pressure drop when the heat flux was increased to 200 W/cm^2 with the results when q" = 100 W/cm^2 in configuration A are shown in Fig. B1. The pressure drop at a heat flux of 200 W/cm^2 was slightly less than that a heat flux of 100 W/cm^2 owing to the increase in fluid temperature itself and the decrease in dynamic viscosity. The rate of the pressure drop according to the change in thermophysical properties was approximately 4.4%. Likewise, when the heat flux was 200 W/cm^2, the total thermal resistance decreased at a rate of MAE = 1.5% owing to the increase in the thermal conductivity of water.

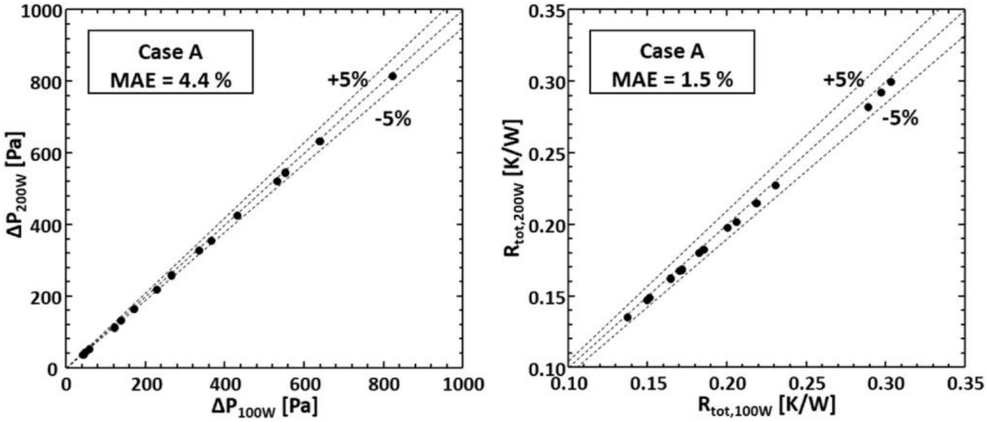

Fig. B1. Comparison of the pressure drop and total thermal resistance when q" = 100W/cm^2 and 200 W/cm^2.

References

[1] V. Venkatadri, B. Sammakia, K. Srihari, D. Santos, A review of recent advances in thermal management in three dimensional chip stacks in electronic systems, J. Electron. Packag. 133 (2011).
[2] W. Qu, I. Mudawar, Experimental and numerical study of pressure drop and heat transfer in a single-phase micro-channel heat sink, Int. J. Heat Mass Tran. 45 (2002) 2549–2565.
[3] H.Y. Zhang, D. Pinjala, T.N. Wong, K.C. Toh, Y.K. Joshi, Single-phase liquid cooled microchannel heat sink for electronic packages, Appl. Therm. Eng. 25 (2005) 1472–1487.
[4] M. Asadi, G. Xie, B. Sunden, A review of heat transfer and pressure drop characteristics of single and two-phase microchannels, Int. J. Heat Mass Tran. 79 (2014) 34–53.
[5] A. Ghahremannezhad, K. Vafai, Thermal and hydraulic performance enhancement of microchannel heat sinks utilizing porous substrates, Int. J. Heat Mass Tran. 122 (2018) 1313–1326.
[6] D.J. Womac, S. Ramadhyani, F.P. Incropera, Correlating equations for impingement cooling of small heat sources with single circular liquid jets, J. Heat Tran. 115 (1993) 106–115.
[7] M.K. Sung, I. Mudawar, Single-phase hybrid micro-channel/micro-jet impingement cooling, Int. J. Heat Mass Tran. 51 (2008) 4342–4352.
[8] M. Chaudhari, B. Puranik, A. Agrawal, Heat transfer characteristics of synthetic jet impingement cooling, Int. J. Heat Mass Tran. 53 (2010) 1057–1069.
[9] J. Kim, Spray cooling heat transfer: the state of the art, Int. J. Heat Fluid Flow 28 (2007) 753–767.
[10] S. Escobar-Vargas, J.E. Gonzalez, D. Fabris, R. Sharma, C. Bash, High heat flux with small scale monodisperse sprays, J. Heat Tran. 134 (2012) 122202.
[11] Y. Hou, Y. Tao, X. Huai, The effects of micro-structured surfaces on multi-nozzle spray cooling, Appl. Therm. Eng. 62 (2014) 613–621.
[12] N. Raja Kuppusamy, R. Saidur, N.N.N. Ghazali, H.A. Mohammed, Numerical study of thermal enhancement in micro channel heat sink with secondary flow, Int. J. Heat Mass Tran. 78 (2014) 216–223.
[13] W.M.A.A. Japar, N.A.C. Sidik, S. Mat, A comprehensive study on heat transfer enhancement in microchannel heat sink with secondary channel, Int. Commun. Heat Mass Tran. 99 (2018) 62–81.
[14] M.M. Nahar, B. Ma, K. Guye, Q.H. Chau, J. Padilla, M. Iyengar, D. Agonafer, Review article: microscale evaporative cooling technologies for high heat flux microelectronics devices: background and recent advances, Appl. Therm. Eng. 194 (2021) 117109.
[15] D. Jung, H. Lee, D. Kong, E. Cho, K.W. Jung, C.R. Kharangate, M. Iyengar, C. Malone, M. Asheghi, K.E. Goodson, H. Lee, Thermal design and management of micro-pin fin heat sinks for energy-efficient three-dimensional stacked integrated circuits, Int. J. Heat Mass Tran. 175 (2021) 121192.
[16] Z. Wan, Y. Joshi, Pressure drop and heat transfer characteristics of pin fin enhanced microgaps in single phase microfluidic cooling, Int. J. Heat Mass Tran. 115 (2017) 115–126.
[17] D. Kong, K.W. Jung, S. Jung, D. Jung, J. Schaadt, M. Iyengar, C. Malone, C.R. Kharangate, M. Asheghi, K.E. Goodson, H. Lee, Single-phase thermal and hydraulic performance of embedded silicon micro-pin fin heat sinks using R245fa, Int. J. Heat Mass Tran. 141 (2019) 145–155.
[18] W. Deng, A. Gomez, Electrospray cooling for microelectronics, Int. J. Heat Mass Tran. 54 (2011) 2270–2275.
[19] Y. Kim, S. Jung, S. Kim, S.T. Choi, M. Kim, H. Lee, Heat transfer performance of water-based electrospray cooling, Int. Commun. Heat Mass Tran. 118 (2020) 104861.
[20] Y. Deng, J. Liu, A liquid metal cooling system for the thermal management of high power LEDs, Int. Commun. Heat Mass Tran. 37 (2010) 788–791.
[21] Y. Xuan, Q. Li, Heat transfer enhancement of nanofluids, Int. J. Heat Fluid Flow 21 (2000) 58–64.
[22] D.B. Tuckerman, R.F.W. Pease, High-performance heat sinking for VLSI, IEEE Electron. Device Lett. 2 (1981) 126–129.
[23] G.M. Harpole, J.E. Eninger, Micro-channel heat exchanger optimization, in: Proc. 7th IEEE Semi-therm Symp., 1991, pp. 59–63.
[24] R.S. Andhare, A. Shooshtari, S.V. Dessiatoun, M.M. Ohadi, Heat transfer and pressure drop characteristics of a flat plate manifold microchannel heat exchanger in counter flow configuration, Appl. Therm. Eng. 96 (2016) 178–189.
[25] F. Battaglia, F. Singer, D.C. Deisenroth, M.M. Ohadi, Experimental characterization of two-phase cooling of power electronics in thermosiphon and forced convection modes, J. Electron. Packag. 143 (2021), 031006.
[26] Y. Peng, Z. Li, S. Li, B. Cao, X. Wu, X. Zhao, The experimental study of the heat transfer performance of a zigzag-serpentine microchannel heat sink, Int. J. Therm. Sci. 163 (2021) 106831.
[27] W. Escher, T. Brunschwiler, B. Michel, D. Poulikakos, Experimental investigation of an ultrathin manifold microchannel heat sink for liquid-cooled chips, J. Heat Tran. 132 (2010).
[28] K.P. Drummond, D. Back, M.D. Sinanis, D.B. Janes, D. Peroulis, J.A. Weibel, S.V. Garimella, A hierarchical manifold microchannel heat sink array for high-heat-flux two-phase cooling of electronics, Int. J. Heat Mass Tran. 117 (2018) 319–330.
[29] D. Back, K.P. Drummond, M.D. Sinanis, J.A. Weibel, S.V. Garimella, D. Peroulis, D.B. Janes, Design, fabrication, and characterization of a compact hierarchical manifold microchannel heat sink array for two-phase cooling, IEEE Trans. Compon. Packag. Manuf. Technol. 9 (2019) 1291–1300.
[30] K.W. Jung, C.R. Kharangate, H. Lee, J. Palko, F. Zhou, M. Asheghi, E.M. Dede, K.E. Goodson, Embedded cooling with 3D manifold for vehicle power electronics application: single-phase thermal-fluid performance, Int. J. Heat Mass Tran. 130 (2019) 1108–1119.

[31] R. van Erp, R. Soleimanzadeh, L. Nela, G. Kampitsis, E. Matioli, Co-designing electronics with microfluidics for more sustainable cooling, Nature 585 (2020) 211–216.
[32] M.A. Arie, A. Shooshtari, M. Ohadi, Air side enhancement of heat transfer in an additively manufactured 1 kW heat exchanger for dry cooling applications, in: 2017 16th IEEE Intersociety Conference on Thermal and Thermomechanical Phenomena in Electronic Systems (ITherm), IEEE, Orlando, FL, 2017, pp. 1–8.
[33] X. Zhang, R. Tiwari, A.H. Shooshtari, M.M. Ohadi, An additively manufactured metallic manifold-microchannel heat exchanger for high temperature applications, Appl. Therm. Eng. 143 (2018) 899–908.
[34] I.L. Collins, J.A. Weibel, L. Pan, S.V. Garimella, A permeable-membrane microchannel heat sink made by additive manufacturing, Int. J. Heat Mass Tran. 131 (2019) 1174–1183.
[35] C.R. Kharangate, W. Libeer, J. Palko, H. Lee, J. Shi, M. Asheghi, K.E. Goodson, Investigation of 3D manifold architecture heat sinks in air-cooled condensers, Appl. Therm. Eng. 167 (2020) 114700.
[36] C.S. Sharma, M.K. Tiwari, B. Michel, D. Poulikakos, Thermofluidics and energetics of a manifold microchannel heat sink for electronics with recovered hot water as working fluid, Int. J. Heat Mass Tran. 58 (2013) 135–151.
[37] D.L. Gee, R.L. Webb, Forced convection heat transfer in helically rib-roughened tubes, Int. J. Heat Mass Tran. 23 (1980) 1127–1136.